Reconstruction of internal gravity wave and turbulence parameters in the stratosphere using GOMOS scintillation measurements

Viktoria F. Sofieva, A.S. Gurvich, Francis Dalaudier, V. Kan

Reconstruction of internal gravity wave and turbulence parameters in the stratosphere using GOMOS scintillation measurements

V. F. Sofieva,[1] A. S. Gurvich,[2] F. Dalaudier,[3] and V. Kan[2]

Received 5 May 2006; revised 16 February 2007; accepted 15 March 2007; published 23 June 2007.

[1] Exploitation of stellar scintillation allows studying air density irregularities in the stratosphere. In this paper, we develop a methodology for reconstruction of internal gravity wave (IGW) and turbulence parameters using scintillation measurements by the Global Ozone Monitoring by Occultation of Star (GOMOS) fast photometers on board the Envisat satellite. The forward model is based on a two-component spectral model of air density irregularities: the first component corresponds to the gravity wave spectrum, while the second one describes locally isotropic turbulence resulting from internal gravity wave breaking. The retrieval of parameters of IGW and turbulence spectra is based on the maximum likelihood method. The developed algorithm is tested on simulated and real data, and its accuracy is assessed. It is shown that the measured scintillation spectra are in good agreement with the proposed model and that structure characteristics and inner and outer scales of the anisotropic component can be reconstructed from scintillation spectra. The developed method can provide information about global distribution of parameters of IGW and turbulence spectra in the stratosphere at altitudes from 25 to 50 km.

Citation: Sofieva, V. F., A. S. Gurvich, F. Dalaudier, and V. Kan (2007), Reconstruction of internal gravity wave and turbulence parameters in the stratosphere using GOMOS scintillation measurements, *J. Geophys. Res.*, *112*, D12113, doi:10.1029/2006JD007483.

1. Introduction

[2] Upward propagating waves and their breaking into turbulence are of fundamental importance for the dynamics and mixing within the middle atmosphere. According to the present theory (cf. the review by *Fritts and Alexander* [2003]), internal gravity waves (IGW) are generated in the troposphere above mountains, above convective zones, and in jet streams. They propagate upward with growing amplitude (caused by decreasing air density) until they reach instability conditions and break down. The turbulence, generated by the breaking IGW, leads to effective turbulent mixing of the stratosphere and to dissipation of kinetic energy into heat at the final step of this process. The wave propagation and breaking produce a drag on the background flow. Since it tends to occur continuously and globally, it affects the global circulation and chemical composition of the middle atmosphere.

[3] The understanding of the global effects of the relatively small-scale gravity waves has improved during the last two decades. It is known now that gravity waves influence the stratospheric circulation [*Holton*, 1983; *Alexander and Rosenlof*, 1996]. Gravity waves also affect ice cloud formation [*Jensen et al.*, 2001] and polar ozone loss [*Carslaw et al.*, 1998; *Dörnbrack et al.*, 2002; *Fueglistaler et al.*, 2003]. It is now understood that gravity waves play an important role in driving the quasi-biennial oscillation [*Dunkerton*, 1997; *Alexander and Holton*, 1997; *Takahashi*, 1996; *Giorgetta et al.*, 2002]. Gravity waves and turbulence are believed to be responsible for the observed reversal of the summer-to-winter temperature gradient in the upper mesosphere and to play an important role in controlling temperatures in the Antarctic ozone hole [*Garcia and Boville*, 1994].

[4] The studies of gravity waves are based on different ground-based, in situ, and satellite measurements (cf. the reviews by *Fritts and Alexander* [2003] and *Wu et al.* [2006]). The important advantage of satellite measurements is their global coverage. Information about gravity waves activity has been obtained from satellite measurements via analysis of the temperature perturbations that gravity waves produce in the atmosphere or radiance perturbations in temperature-sensitive emissions. The shortest vertical wavelength addressable by radio occultation, the technique with the best vertical resolution [*Tsuda et al.*, 2000; *Steiner and Kirchengast*, 2000], is about 1 km. This resolution is sufficient to probe the saturated part of the vertical wave number spectrum [*Steiner and Kirchengast*, 2000]. Lower vertical resolution can give insight in source distributions [*Eckermann and Preusse*, 1999; *Jiang et al.*, 2004a, 2004b]

[1] Finnish Meteorological Institute, Helsinki, Finland.
[2] A. M. Oboukhov Institute of Atmospheric Physics, Moscow, Russia.
[3] Service d'Aeronomie, Verrières-le-Buisson Cedex, France.

0148-0227/07/2006JD007483

or details of the wave fields like the propagation direction [*Preusse et al.*, 2002; *Wu and Zhang*, 2004]. However, measurements from a particular instrument are sensitive to a certain part of the broad gravity wave spectrum in a certain altitude range [*Wu et al.*, 2006].

[5] The satellite observation of stellar scintillations [*Gurvich and Kan*, 2003a, 2003b] is a new approach that allows studying small-scale processes in the stratosphere. The scintillations, or fluctuations of stellar flux intensity measured through the atmosphere with high-frequency devices, are caused by irregularities of air density, and they contain therefore information about small-scale processes in the atmosphere. Scintillations are strongly influenced by gravity waves with vertical scales from few meters to few kilometers, which are of high importance for parameterization of gravity wave effects in general circulation models and in models of climate change. They can provide information about IGW in the altitude range 25–50 km. Furthermore, scintillations can also provide information about gravity wave breaking [*Gurvich et al.*, 2005]. This is one of the least quantified aspects of gravity wave forcing of the middle atmosphere at present [*Fritts and Alexander*, 2003]. The smallest scales addressable by the scintillation method are few meters/a fraction of meter, depending on the sampling rate of a detector.

[6] The scintillation measurements became available with global coverage since the launch of the Envisat satellite in March 2002. The Global Ozone Monitoring by Occultation of Star (GOMOS) instrument on board the Envisat satellite [http://envisat.esa.int/instruments/gomos; *Kyrölä et al.*, 2004; *Bertaux et al.*, 2004] is equipped with two fast photometers with a sampling frequency of 1 kHz, which perform synchronous scintillation measurements at blue (~500 nm) and red (~672 nm) wavelengths. The photometers measure stellar flux passed through the atmosphere continuously as a star sets behind the Earth limb. Previously, stellar scintillation measurements were conducted by Russian cosmonauts on board the space stations SALYUT [*Aleksandrov et al.*, 1990] and MIR [*Gurvich et al.*, 2001a]. Despite the limited amount of occultations performed, these scintillation data allowed the understanding and analysis of statistical and spectral properties of scintillations [*Gurvich et al.*, 2001a, 2001b] and have validated the scintillation theory developed in the study of *Gurvich and Brekhovskikh*, 2001.

[7] Although stellar scintillation data contain information about small-scale processes in the stratosphere, the retrieval of this information is a complicated task because a three-dimensional distribution of air density irregularities is searched from one-dimensional scintillation measurements. The theory developed by *Tatarskii* [1971] allows expression of the wave number spectrum of scintillation along the observation path (one-dimensional) via the integrals from three-dimensional spectrum of air density irregularities, with a weighting function due to the effects of light diffraction. It is possible, in principle, to measure a set of one-dimensional scintillation spectra from observations performed at different angles between the orbital plane and direction to the star and to formulate reconstruction of a three-dimensional spectrum as a tomography problem. However, this requires occultations with different angles of star motion at the same location and time, which is not available from current measurements.

[8] An approach that allows solving the problem of reconstruction of three-dimensional spectrum of air density irregularities using one-dimensional scintillation autospectra was proposed in the study of *Gurvich and Kan* [2003a, 2003b]: the spectrum of the air density irregularities is parameterized, the theoretical relations that connect the three-dimensional spectrum of air density irregularities and one-dimensional scintillation spectrum at observation point are deduced, and the parameters of the spectral model are retrieved via fitting experimental scintillation spectra.

[9] In this work, we develop further this approach and adapt it to the reconstruction of the IGW and turbulence spectra parameters from GOMOS scintillation measurements. In section 2, we describe the forward model, which includes parameterization of the spectrum of air density irregularities and theoretical relations for the scintillation spectra. Section 3 is dedicated to calculation of experimental scintillation spectra. In section 4, we describe the inversion procedure. Uncertainties in the retrieved parameters are discussed in section 5. Results of sample retrievals from GOMOS scintillation measurements are presented in section 6.

2. Forward Model

[10] The forward modeling includes the parameterization of a three-dimensional spectrum of air density irregularities and the computation of the one-dimensional scintillation spectrum at the observation point corresponding to these irregularities. In the following, we present the description of these steps.

2.1. Two-Component Spectral Model of Air Density Irregularities

[11] Scintillations observed in the stellar occultation experiment are caused by air density irregularities. The velocity of the line of sight within the atmosphere is very large during an occultation; this allows using the frozen field approximation with respect to all atmospheric motions. Atmospheric refractivity, $N = n-1$, n being the refractive index, depends on height above the Earth surface h and on radiation wavelength λ. For optical wavelength, the mean refractivity is defined by

$$\langle N(h)\rangle = 77.6 \cdot 10^{-6} \frac{\langle P(h)\rangle}{\langle T(h)\rangle}\left(1 + \left(\frac{\Lambda}{\lambda}\right)^2\right), \qquad (1)$$

where $\langle T(h)\rangle$ is temperature in kelvin, $\langle P(h)\rangle$ is pressure in millibar, and the parameter $\Lambda = 87$ nm describes optical dispersion of air (angular brackets hereafter denote the statistical mean). We will describe the structure of relative fluctuations $\nu = \frac{N-\langle N\rangle}{\langle N\rangle}$ of refractivity via three-dimensional spectral density $\Phi_\nu(\mathbf{k})$, with $\kappa = (\kappa_x, \kappa_y, \kappa_z)$ being a wave vector (z is the vertical coordinate). Following the work of *Gurvich and Kan*, 2003a, we represent Φ_ν as a sum of two

statistically independent components: anisotropic, Φ_W, and isotropic, Φ_K:

$$\Phi_\nu = \Phi_W + \Phi_K. \tag{2}$$

[12] The first component Φ_W corresponds to anisotropic irregularities generated by a random ensemble of internal gravity waves [*Smith et al.*, 1987; *Sidi et al.*, 1988]. For parameterization of this component, we use -5 power law three-dimensional spectrum

$$\Phi_W = C_W \eta^2 \left(\kappa_z^2 + \eta^2 \kappa_\perp^2 + \kappa_0^2\right)^{-5/2} \varphi\left(\frac{k}{\kappa_W}\right)$$
$$k^2 = \eta^2 \kappa_\perp^2 + \kappa_z^2, \quad \kappa_\perp^2 = \kappa_x^2 + \kappa_y^2, \tag{3}$$

where C_W is the structure characteristic defining the power of the anisotropic irregularities, η is the anisotropy coefficient defined as a ratio between the characteristic vertical and horizontal wave numbers of Φ_W [*Gurvich and Chunchuzov*, 2005], and κ_0 and κ_W are the wave numbers corresponding to the outer and the inner vertical scales that bound the spectrum of air density irregularities at low and high wave numbers, respectively. The spectrum Φ_W is assumed to be isotropic in the horizontal plane. The function $\varphi(\xi)$ in equation (3) goes smoothly from 1 ($\xi \ll 1$) to 0 ($\xi \gg 1$) and describes the decay of the anisotropic spectrum at $k > \kappa_W$; it is usually taken as Gaussian, $\varphi(\xi) = \exp(-\xi^2)$, for convenience of analytical calculations. According to the papers of *Gurvich and Kan* [2003a, 2003b] and *Gurvich and Chunchuzov* [2005], $1/\kappa_W$ has the same order of magnitude as the buoyancy scale.

[13] The associated one-dimensional vertical spectrum $V(\kappa_z) = 2\pi \int_0^\infty \Phi_W(\kappa_z, \kappa_\perp)\, \kappa_\perp d\kappa_\perp$ can be approximated for $\kappa_0 \ll \kappa_z \ll \kappa_W$ by $V(\kappa_z) \approx C_W \frac{2\pi}{3} \kappa_z^{-3}$. It corresponds to the saturated gravity waves model [*Smith et al.*, 1987]

$$V_{\delta T/T} = A \frac{\omega_{\mathrm{BV}}^4}{g^2} \kappa_z^{-3}, \tag{4}$$

thus giving the following theoretical estimate for C_W:

$$C_W = \frac{3}{4\pi} A \frac{\omega_{BV}^4}{g^2}, \tag{5}$$

where ω_{BV} is the Brunt-Väisälä angular frequency, g is the acceleration of gravity, and $A \approx 0.1$ is the constant in the model of saturated gravity waves [*Tsuda et al.*, 1991].

[14] The spectral model of the anisotropic irregularities (3) differs from that used in the work of *Gurvich and Kan* [2003a, 2003b] by inclusion of an outer-scale characterization. The characteristic wave number κ_0 defines the low wave number limit of the k^{-5} spectrum (see Figure 1 in the paper of *Gurvich and Chunchuzov* [2005]). In this sense, the value of $\frac{2\pi}{\kappa_0}$ can be taken as an estimate of the outer scale of the anisotropic spectrum Φ_W, analogously to the outer scale of turbulence. The expression for the outer-scale characterization is different from that in the study of *Gurvich and Chunchuzov* [2005] in order to simplify the calculation of scintillation spectra. The anisotropy coefficient η is assumed to be constant in equation (3). The validity of this assumption is discussed further in section 2.3. Although the three-dimensional spectral model for IGW is more complicated, the model (3) takes into account all the important physical parameters controlling the shape of scintillation spectra. It has been already successfully applied for interpretation of stellar scintillation spectra [*Gurvich and Chunchuzov*, 2005].

[15] The second component of the spectrum of air density irregularities (2), Φ_K, corresponds to isotropic irregularities generated by turbulence, which appear as a result of internal wave breaking and/or different instabilities of atmospheric motions. For its parameterization, we adopt the Oboukhov-Corssin model of locally isotropic turbulence [*Monin and Yaglom*, 1975]:

$$\Phi_K(k) = 0.033 C_K k^{-11/3} \exp\left(-(k/\kappa_K)^2\right)$$
$$k^2 = \kappa_x^2 + \kappa_y^2 + \kappa_z^2 \tag{6}$$

where C_K is the structure characteristic, and κ_K is the inner scale of isotropic irregularities. The structure characteristic C_K is proportional to $\varepsilon_\nu/\varepsilon^{1/3}$, where ε_ν is the rate of dissipation of refractivity fluctuations, and ε is the kinetic energy dissipation rate. $1/\kappa_K$ is proportional to the Kolmogorov scale $l_K = \nu_{\mathrm{a}}^{3/4}\, \varepsilon^{-1/4}$, where ν_{a} is the molecular kinematic viscosity for air. The one-dimensional spectrum corresponding to equation (6) follows the well-known $-5/3$ power law.

2.2. Scintillation Spectra in Stellar Occultation

[16] The observations of stellar scintillation are performed in the limb-viewing geometry (for illustration, see, for example, Figure 1 in the paper of *Gurvich et al.* [2005]). The photometers measure stellar flux passed through the atmosphere continuously as a star sets behind the Earth limb. In observations of stars through the atmosphere, each component of air density irregularities produces scintillation in the observation plane. For weak scintillations, the spatial scintillation spectrum is the sum of anisotropic and isotropic components. The theoretical relations that allow calculating a one-dimensional spectrum of relative fluctuations of intensity at the observation plane from the given spectrum of air density irregularities were developed in the studies of [*Gurvich and Brekhovskikh*, 2001; and *Gurvich and Kan* 2003a]. They have been obtained in the phase-screen approximation under the weak scintillation assumption, i.e., under the assumption of small RMS relative fluctuations of light intensity [*Tatarskii*, 1971].

[17] In the framework of the phase-screen approximation, the effect of the extended atmosphere on the light wave passing through it is replaced by that of a virtual phase screen located in the ray perigee (the nearest to the Earth surface) point. The phase screen changes the optical path length by the value

$$\Psi = \int_{\mathrm{ray}} N(\mathbf{r}) dl, \tag{7}$$

which we will call the eikonal increase. Integration in equation (7) is performed along the ray path. For the exponential dependence of the mean refractivity $\langle N \rangle$ on

altitude h, $\langle N\rangle = \langle N(h_0)\rangle \exp(-(h - h_0)/H(h_0))$, the mean value of Ψ can be approximated by [*Gurvich and Brekhovskikh*, 2001]:

$$\langle\Psi\rangle \approx \sqrt{2\pi a_E H(h_p)}\langle N(h_p)\rangle, \tag{8}$$

where a_E is the Earth's radius, and $H(h_p)$ is the atmospheric scale height at a ray perigee point h_p.

[18] Eikonal fluctuations $\Psi = \Psi - \langle\Psi\rangle$ are described by the two-dimensional spectral density F_Ψ defined on the phase screen, which is related with Φ_ν by the equation [*Gurvich and Brekhovskikh*, 2001]:

$$F_\Psi(\kappa_z, \kappa_y) = \frac{\langle\Psi\rangle^2}{\sqrt{1+\kappa_z^2H^2}} \cdot \int_{-\infty}^{\infty} \Phi_\nu(\kappa_x, \kappa_y, \kappa_z)\exp\left(-\frac{a_E H\kappa_x^2}{1+\kappa_z^2H^2}\right)d\kappa_x. \tag{9}$$

[19] The integration in equation (9) for the Gaussian decay at large wave numbers $\varphi(\xi) = \exp(-\xi^2)$ in the expression for Φ_ν results in the following analytical formula for $F_\Psi(\kappa_z, \kappa_y)$:

$$\frac{F_\Psi(\kappa_z,\kappa_y)}{\langle\Psi\rangle^2} = C\frac{\sqrt{\pi}\eta^2\sqrt{Z}U(1/2,(3-\mu)/2,Z)}{\sqrt{a_E H+\eta^2(1+\kappa_z^2H^2)/\kappa_\infty^2}}\rho^{-\mu}\exp\left(-\frac{\rho^2}{\kappa_\infty^2}\right)$$
$$\rho^2 = \kappa_z^2 + \eta^2\kappa_y^2 + \kappa_0^2$$
$$Z = \frac{\rho^2}{\kappa_\infty^2}\left(1+\frac{a_E H\kappa_\infty^2}{\eta^2(1+k_z^2H^2)}\right) \tag{10}$$

[20] For the spectrum of anisotropic air density irregularities (3), $C = C_W$, $\mu = 5$, and $\kappa_\infty = \kappa_W$, while for the isotropy spectrum (6), $C = C_K$, $\eta = 1$, $\kappa_0 = 0$, $\mu = 11/3$, and $\kappa_\infty = \kappa_K$ should be taken in equation (10). $U(a, b, \zeta)$ in equation (10) is the confluent hypergeometric function.

[21] At the observation plane, located at a distance L from the ray perigee, the two-dimensional spectrum of relative fluctuations of light intensity $F_J(\kappa_y, \kappa_z)$ is related with F_Ψ by the formula

$$F_J(\kappa_z,\kappa_y) = \Xi(\kappa_z,\kappa_y)F_\Psi\left(\frac{\kappa_z}{q},\kappa_y\right), \tag{11}$$

where the factor $\Xi(\kappa_z, \kappa_y)$ takes into account the diffraction of light, the refractive attenuation q, the effects of chromatic aberration [*Dalaudier et al.*, 2001], and the averaging of scintillations over the aperture of the receiver. The explicit expression for Ξ is given by equation (16) in the paper of *Gurvich and Kan* [2003a] and by equation (21) in the paper of *Gurvich and Brekhovskikh* [2001].

[22] Finally, to find the one-dimensional scintillation spectrum for comparison with experimental spectra, we integrate

$$V(\kappa,\alpha) = \int_{-\infty}^{+\infty} F_J(-k_n\sin\alpha + \kappa\cos\alpha, k_n\cos\alpha + \kappa\sin\alpha)dk_n. \tag{12}$$

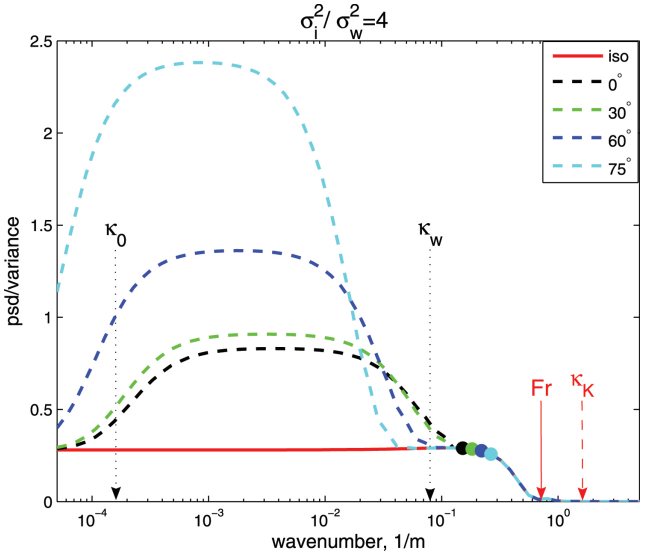

Figure 1. Scintillation spectra for the mixture of anisotropic and isotropic inhomogeneities for different angles α of star motion. The ratio of isotropic and isotropic scintillation variances is $\sigma_i^2/\sigma_w^2 = 4$. The component corresponding to the isotropic irregularities is referred to as "iso." The wave numbers corresponding to the Nyquist frequency are indicated by colored disks. Arrows indicate κ_0, κ_W, and κ_K, and the wave number corresponding to the Fresnel scale (Fr).

[23] Here κ is the wave number along the projection of the satellite trajectory on the observation plane $x = L$, and α is the angle between the direction of the apparent motion of the observed star and the local vertical at the ray perigee point. $\alpha = 0°$ in vertical (in orbital plane) occultations; $\alpha > 0°$ in oblique (off orbital plane) occultations, with the limit $\alpha = 90°$ in case of purely horizontal occultations. The integration in equation (12) is performed numerically.

[24] The equations (10), (11), and (12) constitute the kernel of the forward model for retrieval of IGW and turbulence parameters. Apart from the parameters of air density irregularities, the forward model contains other implicit parameters (the dilution factor, the chromatic separation, and the mean eikonal value), which depend on the mean refractivity. In retrievals, they are calculated using ECMWF air density at the occultation location.

2.3. How Many Parameters can be Retrieved From the GOMOS Scintillations?

[25] Examples of model scintillation spectra computed with the aid of equations (10), (11), and (12) are presented in Figure 1 for different angles of star motion α. The anisotropy coefficient $\eta = 30$ is fixed in these calculations (see below). The ratio of variances of anisotropic σ_w^2 and isotropic σ_i^2 components is chosen as $\sigma_i^2/\sigma_w^2 = 4$ in this example. The power spectral density presented in Figure 1 is normalized on the total scintillation variance. Because of the presence of an outer scale in the spectra of anisotropic inhomogeneities, the spectral density of scintillation decreases at low wave numbers. However, such a decrease has a small impact on the value of the total scintillation variance $\sigma_w^2 + \sigma_i^2$ because it takes place within a quite

narrow spectral band. As noted by *Gurvich and Kan* [2003b], the spectral density of the anisotropic component increases with growing α. This is accompanied by shifting the wave number range of the anisotropic component toward small wave numbers, so that σ_w^2 is independent of α. As noted in the study of *Gurvich and Chunchuzov* [2005], such spectral dependence on α at low wave numbers is valid for $\cos\alpha > 1/\eta$. When this condition is violated, the one-dimensional spectral density at small wave numbers tends to some constant magnitude, which does not depend on an outer scale.

[26] The largest wave number that is observable in experimental scintillation spectra is dictated by the discretization step of the photometer data. Since the sampling frequency of the GOMOS fast photometer is 1 kHz, the smallest wavelength that can be obtained is usually larger than both the Fresnel scale ($\sim$1.4 m for GOMOS) and the Kolmogorov scale. It is illustrated in Figure 1, where the colored disks indicate the wave numbers κ_{Ny} corresponding to the Nyquist frequency ($\kappa_{\mathrm{Ny}} = 2\pi f_{\mathrm{Ny}}/v_{\mathrm{p}}$, where f_{Ny} is the Nyquist frequency and v_{p} is the ray perigee velocity) and the arrows indicate the wave numbers corresponding to the Fresnel scale and to the Kolmogorov scale. The spectral density of isotropic scintillation is practically constant for wave numbers $\kappa < \kappa_{\mathrm{Ny}}$; its magnitude depends on ratio between the Fresnel scale and the Kolmogorov scale. Since it is impossible to retrieve any information about the Kolmogorov scale from the GOMOS scintillations due to limited sampling frequency, we use the assumption that the Kolmogorov scale is much smaller than the Fresnel scale, i.e., $Fr \cdot \kappa_K \to \infty$.

[27] Stellar scintillation observations [*Aleksandrov et al.*, 1990; *Grechko et al.*, 1992] have shown that the irregularities of the vertical scales larger than tens of meters are strongly stretched along the Earth's surface. The analysis of the scintillation spectra obtained from these observations has shown that the corresponding anisotropy factor η is certainly larger than 30. The numerical simulation [*Gurvich and Brekhovskikh*, 2001] has shown that the spectral density of scintillation depends weakly on the value of η for $\eta > 30$ and $\cos\alpha > 1/\eta$ (for illustration, see Figures 3 and 4 in the work of *Gurvich and Brekhovskikh* [2001]). Under these circumstances, keeping the anisotropy coefficient as a parameter for fitting (together with C_K, C_W, κ_W, and κ_0) makes the problem of the parameters reconstruction ill-posed. Therefore, in order to decrease the number of retrieved parameters, we assume $\eta = 30$ in the model spectral density Φ_W in equation (3).

[28] For very oblique occultations (with $\cos\alpha \to 0$), the assumption on weak dependence of scintillation spectra on the anisotropy coefficient is violated. Furthermore, the model Φ_W with the constant anisotropy factor η certainly requires a revision in this case. As a possible improvement, one can use the models with varying anisotropy [*Gurvich*, 1995; *Gurvich*, 1997; *Dalaudier and Gurvich*, 1997]. In this work, we will not consider such occultations.

[29] Four parameters, the structure characteristics C_K of turbulence, the structure characteristics C_W, the inner scale κ_W, and the outer scale κ_0 of the IGW component, can be retrieved from the GOMOS scintillation measurements. It is preferable to select occultations that are sufficiently oblique. The shifting of the spectrum of anisotropic scintillations toward low-frequency domain for oblique occultations results in a better separation of the scintillation components. The horizontal plateau at high wave numbers observed in scintillation spectra in oblique occultations (Figure 1) significantly improves the retrieval accuracy of the structure characteristic C_K. The increase of the spectral density of anisotropic scintillations and the simultaneous decrease of isotropic scintillation spectral density with growing α (due to shifting of isotropic scintillation to high-frequency domain and their damping by filters) [*Kan*, 2004] prompt using oblique occultations, especially in cases when the isotropic component dominates in scintillation spectra.

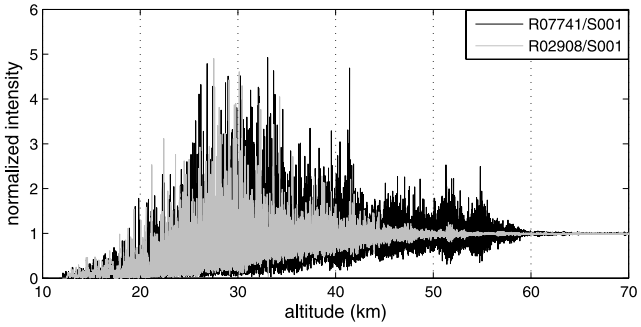

Figure 2. Photometer signals by the GOMOS red photometer in occultations R07741/S001 (62°S, 7°E, 23 August 2003, 23:51 UTC) and R02908/S001 (35°S, 106°W, 20 September 2002, 07:01 UTC).

[30] The altitude range for the IGW and turbulence parameters retrieval is expected to be $\sim$25–50 km. The lower limit is dictated by the weak scintillation assumption used in the forward model. Usually, scintillation becomes strong at altitudes below 25–30 km. The upper altitude for the parameter reconstruction is limited by the scintillation strength, and it is usually $\sim$50 km for GOMOS fast photometers. The analysis of scintillation variance has shown that the scintillations significantly exceed instrumental noise at $\sim$50 km in occultations of stars that are brighter than of visual magnitude 1.6. Usually, amplitude of scintillation is large enough also at altitudes >50 km (an example is shown in Figure 2, occultation R07741/S001). In such cases, retrievals of the parameters of the spectral model can be performed at higher altitudes.

3. Experimental Scintillation Spectra

[31] In this work, we used scintillation measurements by the GOMOS red photometer in oblique occultations. For calculation of experimental spectral densities, 3-s samples are used. Each photometer sample was normalized by its mean value, was detrended in order to remove slow variations caused by absorption, scattering, and refractive dilution, and was apodized. The estimates of experimental spectral density are calculated by smoothing the periodogram obtained by FFT (we use Hanning window for the smoothing). The smoothing applied is analogous to that used in the studies of *Gurvich et al.* [2005] and *Gurvich and Chunchuzov* [2005]. The center of the lowest-frequency window is $f_1 = 3/T_0$, and its width is $5/T_0$. The width of each subsequent window increases by $2/T_0$, while its central

frequency coincides with the upper-frequency bound of the previous one. Thus the width of the spectral window progressively increases with frequency. The frequency grid is chosen in such a way gives better smoothing at high frequencies and preserves the necessary spectral resolution at low frequencies.

[32] The accuracy of the experimental spectral density can be estimated as follows. For each periodogram value P_i, the quantity $(2\frac{P_i}{P(f)})$, where $P(f)$ is the true value of power spectral density at frequency f, has the $\chi^2(2)$ distribution with 2 degrees of freedom [*Yaglom*, 1987]. Therefore, the periodogram estimate has the mean $\langle P_i \rangle = P(f)$ and the variance $\mathrm{var}(P_i) = s_i^2 = P^2(f)$. The periodogram values are statistically independent for a stationary stochastic process; therefore the variance s^2 of the experimental spectral density $\hat{P}(f)$ can be estimated by taking into account averaging within the spectral window:

$$s^2 = \sum_{i=1}^{N_{\mathrm{window}}} s_i^2 w_i^2 = \sum_{i=1}^{N_{\mathrm{window}}} P^2(f) w_i^2, \tag{13}$$

where w_i are weights of the spectral window used for periodogram averaging ($\sum_{i=1}^{N_{\mathrm{window}}} w_i = 1$). In practical calculation, we used equation (13) with replacing unknown true spectral density $P(f)$ by its experimental estimate P_i. Typically, the uncertainty of the experimental spectral density is ~50% at the lowermost wave numbers and decreases with increasing wave number. At higher wave numbers, the uncertainty is 10–15%. Because of the applied periodogram smoothing, the errors corresponding to adjacent frequencies are slightly correlated. If one considers the computed experimental spectrum as a measurement vector, its uncertainty can be characterized by the covariance matrix **S** with the diagonal elements defined by equation (13). Because of the applied smoothing, the matrix **S** is tridiagonal, with off-diagonal elements that are computed analogously

$$s_{i,i+1}^2 = \sum_{j \in (\mathrm{window}(i) \cap \mathrm{window}(i+1))} P_j^2 w_j^2. \tag{14}$$

The off-diagonal elements are ~4 times smaller at all frequencies except for lowermost ones.

[33] The wave numbers associated with the measured spectrum are $\kappa_j = 2\pi f_j / v_{\mathrm{p}}$, where f_j are frequencies and v_{p} is the ray perigee velocity. The wave number spectrum is related with the frequency spectrum by $V(f)\mathrm{d}f = V(\kappa)\mathrm{d}\kappa$, which completes the calculation of the experimental spectral density $V^{\mathrm{meas}}(\kappa_j)$.

4. Algorithm for IGW and Turbulence Parameter Retrieval

4.1. Basic Algorithm

[34] Since the model spectrum of isotropic scintillation is flat at the wave numbers available from the GOMOS scintillations, we can consider it as a constant with a spectral density V_{iso}. This simplification reduces significantly the computing time. As it was already discussed in section 2.3, we use the model with constant anisotropy $\eta = 30$. The forward model (theoretical scintillation spectrum) can be written in the form:

$$V^{\mathrm{mod}}(\kappa) = C_K V_{\mathrm{iso}}(\kappa) + C_W V_{\mathrm{aniso}}(\kappa, \kappa_W, \kappa_0), \tag{15}$$

where κ is a wave number, and V_{iso} and V_{aniso} are isotropic and anisotropic components of the scintillation spectrum, respectively. C_K, C_W, κ_W, and κ_0 are the four parameters to reconstruct. Since the high-frequency part of the experimental spectra is modified by the aliasing effect in the vicinity of the Nyquist frequency, this modification is applied also to the modeled scintillation spectra.

[35] The inverse problem of the IGW and turbulence parameter retrieval can be written in the form

$$\mathbf{V}^{\mathrm{meas}} = \mathbf{V}^{\mathrm{mod}} + \boldsymbol{\delta} = C_K \mathbf{V}_{\mathrm{iso}} + C_W \mathbf{V}_{\mathrm{aniso}}(\kappa_W, \kappa_0) + \boldsymbol{\delta}, \tag{16}$$

where $\mathbf{V}^{\mathrm{meas}}$ is the vector corresponding to the measured spectrum, $\mathbf{V}^{\mathrm{mod}}$ is the vector corresponding to the modeled spectrum, and $\boldsymbol{\delta}$ is the vector representing noise in the experimental data.

[36] The retrieval of four parameters C_K, C_W, κ_W, and κ_0 is based on the standard maximum likelihood method. We assume that the measurement noise is a Gaussian random variable with the zero mean and the covariance matrix **S** defined by equations (13) and (14). Although the uncertainty of experimental spectra has χ^2 distribution, it can be safely approximated by a Gaussian distribution because the $\chi^2(m)$ distribution with m degrees of freedom is asymptotically Gaussian for large m. In this case, the maximum likelihood method is equivalent to minimization of χ^2 statistics:

$$\chi^2 = (C_K \mathbf{V}_{\mathrm{iso}} + C_W \mathbf{V}_{\mathrm{aniso}}(\kappa_W, \kappa_0) - \mathbf{V}^{\mathrm{meas}})^T \cdot \mathbf{S}^{-1} (C_K \mathbf{V}_{\mathrm{iso}} + C_W \mathbf{V}_{\mathrm{aniso}}(\kappa_W, \kappa_0) - \mathbf{V}^{\mathrm{meas}}). \tag{17}$$

[37] It is possible, in principle, to use advanced methods such as the Markov chain Monte Carlo (MCMC) method that avoids the assumption of a Gaussian distribution of noise [*Tamminen*, 2004]. However, these methods are time consuming and therefore cannot be used for operational retrievals.

[38] For minimization, we used a combination of linear and nonlinear optimization because the modeled spectrum depends linearly on structure characteristics C_K and C_W. The nonlinear fit of two parameters κ_W and κ_0 is performed using the Levenberg-Marquardt algorithm [*Press et al.*, 1992], while the parameters C_K and C_W are calculated using the linear weighted least squares method at each iteration. Such combination of linear and nonlinear optimization allows significant reduction of the computing time (note that derivatives of the objective function (17) with respect to parameters κ_W and κ_0 are evaluated numerically) and increases the rate of convergence. The minimum is achieved typically in less than 10 iterations for altitudes 30–45 km.

[39] The quality of the inversion can be characterized by the normalized χ^2 statistics and residuals $R(\kappa_j) = V^{\mathrm{meas}}(\kappa_j) - V^{\mathrm{mod}}(\kappa_j)$. The normalized χ^2_{norm} statistics is defined as

$$\chi^2_{\mathrm{norm}} = \frac{1}{N_{\mathrm{w}} - N_{\mathrm{param}}} \chi^2, \tag{18}$$

where N_w is the number of measurements (number of wave numbers), N_{param} is the number of retrieved parameters ($N_{param} = 4$ in our case), and χ^2 is defined by equation (17). If the model describes well the experimental data and the measurement noise is properly defined, $\chi^2_{norm} \approx 1$ and residuals are close to white noise.

[40] The comparison of experimental and modeled scintillation spectra has shown that using equation (9) at wave numbers $k > \kappa_W$ leads to unsatisfactory fit at large wave numbers (residuals are biased at wave numbers close and larger than κ_W, and $\chi^2_{norm} \approx 2-3$). However, replacing the Gaussian factor in equation (9), $\exp(-(k/\kappa_W)^2)$ by the first term of its series expansion, $\frac{1}{1+(k/\kappa_W)^2}$, improves the agreement between modeled and experimental scintillation spectra: Residuals become close to white noise and $\chi^2_{norm} \approx 1$ typically.

4.2. Filtering Quasiperiodic Structures

[41] Experimental spectra often exhibit large peaks that appear on the background of the smooth scintillation spectrum. The appearance of these peaks seems to be related with quasiperiodic disturbances in the atmospheric density and temperature field. Such peaks are observed simultaneously in spectra of both GOMOS fast photometer signals; they were observed in previous scintillation measurements on board the MIR station [*Gurvich and Chunchuzov*, 2005], too. The quasiperiodic disturbances are not consistent with the model of a random ensemble of internal gravity waves that we aim to parameterize. Therefore we applied filtering to the quasiperiodic structures by using a two-step inversion. For the first step, the retrieval is performed as usual, providing the modeled (smooth) spectrum V_{mod}. Then we detect those points of the experimental spectrum, which have very low probability of appearance that is less than 0.1%. These points are not used in the second step of the inversion, which is performed in the same way as the first one.

[42] The probability of appearance of a particular value of spectral density can be estimated by using the fact that the quantity $\left(2N_{window}\frac{\hat{P}(\kappa)}{P(\kappa)}\right)$ has χ^2 distribution with $2N_{window}$ degrees of freedom. Here $P(\kappa)$ and $\hat{P}(\kappa)$ are the true and experimental values of power spectral density at the wave number κ, and N_{window} is the effective number of periodogram in the spectral window used for estimating the experimental spectrum $\hat{P}(\kappa)$ (for the Hanning window, it is approximately $\frac{2}{3}$ of the number of independent spectral estimations in the window). In practice, the experimental spectrum $V^{meas}(\kappa_j)$ is used for $\hat{P}(\kappa)$, and the model spectrum $V^{mod}(\kappa_j)$ retrieved at the first step is used for $P(\kappa)$.

[43] The two-step inversion is illustrated in Figure 3. Two very large values of spectral density at wave number $\sim$0.01 m^{-1}, which have the probability of appearance <0.1%, are excluded at the second step. The value of the fitted structure characteristic C_K remains practically unchanged, while the values of other retrieved parameters change by 10–30%. The inner and outer vertical scales l_W and L_0 displayed in Figure 3 are defined as $l_W = \frac{2\pi}{\kappa_W}$, $L_0 = \frac{2\pi}{\kappa_0}$.

[44] The results of available retrievals have shown that frequency of outlier appearance due to quasiperiodic structures can be significantly different, depending on altitude, location, and season.

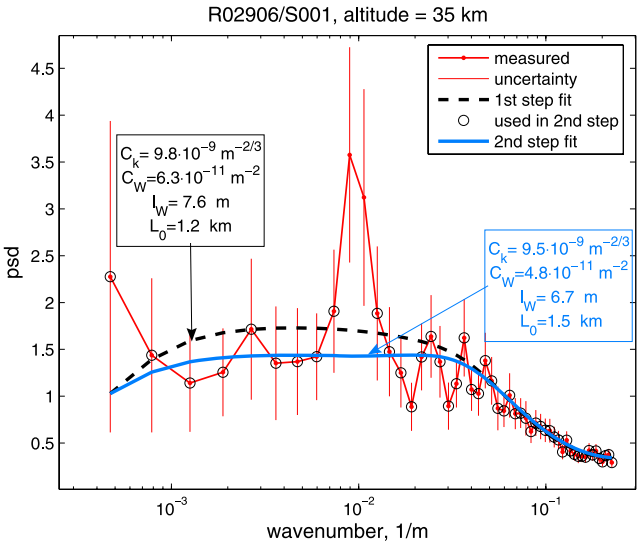

Figure 3. Illustration of the retrieval in two steps. Red thin line: the experimental (measured) spectrum. Black bold dashed line: the fit using all points of the measured spectrum, the first step fit (the values of retrieved parameters are given in the black box). Blue bold solid line: the fit after removal of two outliers (the points used in the retrieval are marked by black circles), the second step fit (the values of retrieved parameters are given in the blue box).

4.3. Examples of Retrievals

[45] The examples of retrievals at several altitudes are shown in Figures 4 and 5, for occultations R02908/S001 ($\alpha = 67°$) and R07741/S001 ($\alpha = 40°$), respectively. The photometer data for these two occultations are shown in Figure 2. The retrievals were performed in two steps. The points that were used in the second step are marked by black circles. If no points are marked, the inversion was performed in one step (no outliers found). The values of retrieved parameters are also shown in the figures. First of all, it can be noted that the fit (model) is in a good agreement with the experimental spectra not only visually but also in terms of the inversion statistics: $\chi^2_{norm} \approx 1$ in these retrievals. The outer scale is clearly observed in the scintillation spectra of R02908/S001 at altitudes 30 and 35 km, but it is weakly observed at altitudes 40 and 45 km.

[46] It can be noticed that the structure of air density irregularities (as well as the scintillation spectra) is quite different in these two occultations at altitudes above 35 km. The anisotropic component is dominant over the isotropic one in the scintillation spectra for R02908/S001 at wave numbers smaller than κ_W, while the isotropic component strongly dominates in R07741/S001 at altitudes 40 and 45 km. Such domination indicates strongly developed turbulence at these altitudes for R07741/S001 (note that the scintillation variance is more than 4 times larger than in R02908/S001 at these altitudes). Also, the anisotropic component is significantly stronger in R07741/S001 compared with R02908/S001 at all altitudes: The structure characteristic C_W is more than 4 times larger. The internal gravity waves seem to reach instability conditions at altitudes above 35 km, where intensive breaking results in

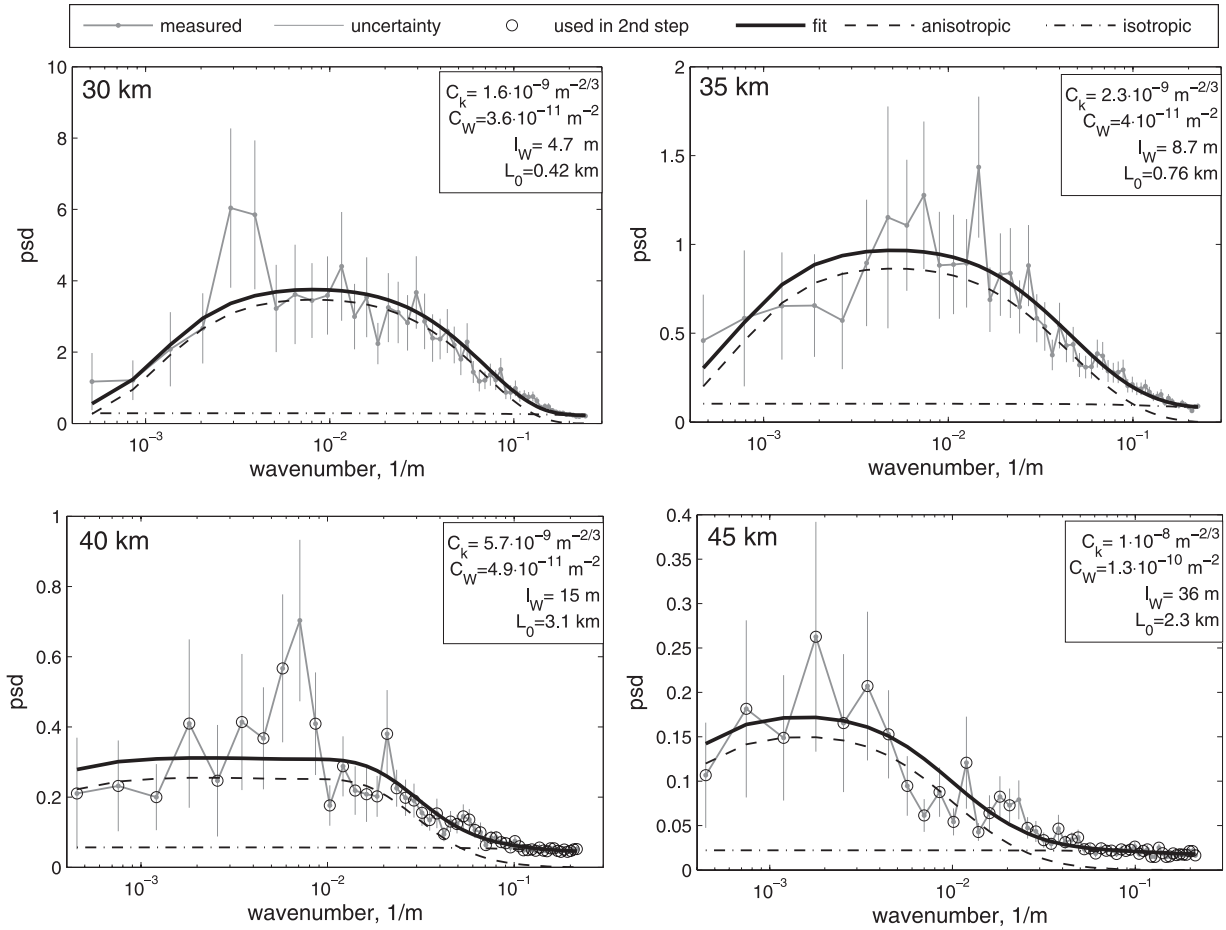

Figure 4. Retrieval results for R02908/S001 (α = 67°, 35°S, 106°W, 20 September 2002) at selected altitudes. The retrieval was performed in two steps. The points that were used in the second step are marked by black circles. No points marked means that the inversion was performed in one step (no outliers found).

turbulence, clearly seen in scintillation spectra for R07741/S001.

[47] For occultation R07741/S001, the retrievals of the anisotropic component parameters are of poor quality at altitudes 40 and 45 km because the anisotropic component is masked by the isotropic one. In case of strong turbulence, selection of occultations with larger obliquity angles would improve accuracy of the retrievals of anisotropic component parameters as discussed in section 2.3.

5. Error Analysis

[48] The statistical error of the retrieved parameters caused by uncertainties in experimental spectra can be estimated using the Jacobian provided by the Levenberg-Marquardt algorithm. Given the Jacobian matrix $\mathbf{J}$: $J_{i,n} = \frac{\partial V^{\mathrm{mod}}(k_i)}{\partial p_n}$, where p_n denotes the retrieved parameters (n = 4), the covariance matrix of the retrieval errors can be determined as

$$\mathbf{C}_P = \left(\mathbf{J}^T\mathbf{S}^{-1}\mathbf{J}\right)^{-1}, \tag{19}$$

where $\mathbf{S}$ is the covariance matrix of the noise in measurements, i.e., the covariance matrix of experimental spectral density uncertainties defined by equations (13) and (14). However, the error estimates (19) can be inaccurate if the inverse problem is strongly nonlinear or the measurement noise/modeling error is improperly estimated. To evaluate the quality of the linearized error estimates (19), we assumed certain IGW and turbulence parameters, simulated the scintillation spectra in the wave number grid of real measurements, added noise that has statistical properties discussed in section 3, and performed the reconstruction of parameters using the simulated spectral density data. We performed 100 Monte Carlo runs with different noise realizations and compared the deviations from the simulation input parameters with the error estimates given by the diagonal elements of equation (19). Figure 6 shows the histograms of relative deviations of the retrieved parameters from the true ones. The black dashed lines are 0.16 and 0.84 percentiles of the deviations; they give robust estimates of the experimental RMS error. The solid vertical lines indicate $\pm 1\sigma$ intervals obtained from the error estimates (19). Taking into account nonsymmetric distribution of the experimental deviations, one can conclude that equation (19) gives acceptable error estimates. The retrieval errors that are associated with the uncertainty of the experimental spectral density are $\sim$5% for C_K, 7–12% for C_W and l_W, and $\sim$50–70% for L_0.

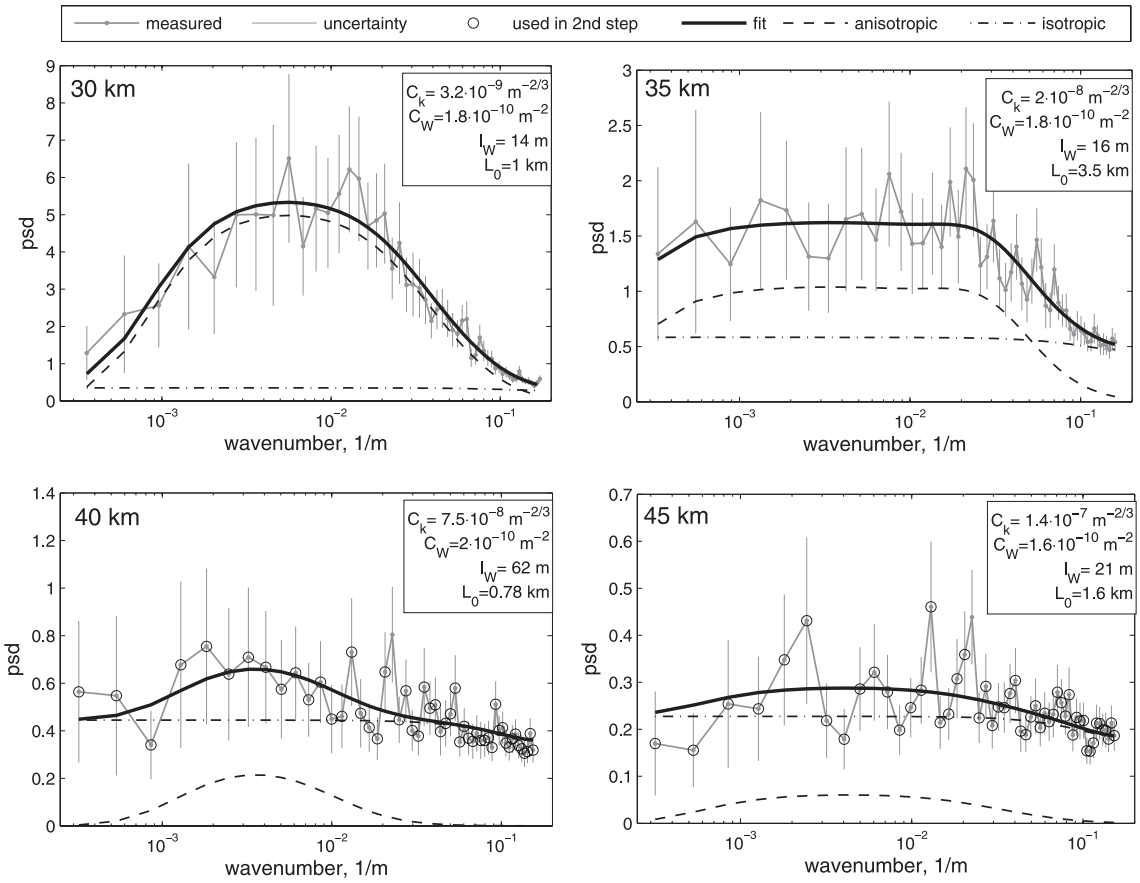

Figure 5. Retrieval results for R07741/S001 (α = 40°, 62°S, 7°E, 23 August 2003). Line notations are as in Figure 4.

[49] The numbers above give only "average" estimates of retrieval accuracy in terms of inversion statistics. The quality of the parameter reconstruction depends on the shape of a scintillation spectrum. A strong turbulent component is reconstructed significantly better than a weak one, which can be almost not observed on a noisy background. The length of the almost-horizontal part of the scintillation spectra at high wave numbers, which depends on obliquity of occultations and on the inner scale l_W, also affects the quality of C_K reconstruction. A well-revealed outer scale is retrieved with a better accuracy than a weakly detected one. The retrieval of the outer scale is the most problematic. The uncertainty of the spectral density estimates is largest at low wave numbers. Additionally, the detrending procedure also contributes to the uncertainty of the outer scale [*Gurvich and Chunchuzov*, 2005]. Although the objective function (17) typically has a single minimum, it is very broad and strongly skewed on the outer-scale axis. This defines the large retrieval error, which has a non-Gaussian distribution. Furthermore, if the outer scale is weakly pronounced in the scintillation spectrum, the convergence criterion can be reached before the real minimum is found.

[50] Another indicator of the quality of retrievals from real data is the normalized χ^2_{norm} statistics. As it was mentioned in section 4.1, $\chi^2_{\text{norm}} \approx 1$ in majority of retrievals in the altitude range of 30–45 km. It means that the forward model describes well the experimental spectra, and the uncertainty of the experimental spectral density is well characterized. The quality of fitting worsens at altitudes below 30 km and above 45 km. The shape of the experimental spectra below 30 km differs from that predicted by the model at large wave numbers because the hypothesis of weak scintillations is violated at these altitudes. At higher altitudes, the outer scale is often not revealed, and χ^2_{norm} increases accordingly.

[51] The uncertainties in retrieved parameters due to inherent properties of the method (for example, due to assumptions about spectra of air density irregularities and assumptions on values of nonretrieved parameters) cannot be estimated in the way described above; therefore the methodological inaccuracies are not covered by the presented error estimates.

[52] In future analyses of climatological patterns of IGW activity by using the discussed method, it is important to take into account that stellar scintillations do not allow to observe the atmosphere from the IGW intrinsic frame of reference. The influence of background winds (which may result in modification of observed IGW wave number spectra) and of "observational filter" by the instrument imposed on the broad GW spectrum [*Alexander*, 1998] should be taken into account.

6. Some Results of Parameter Retrievals

[53] In this section, we show some exemplary retrieval results. Global distribution of the IGW and turbulence

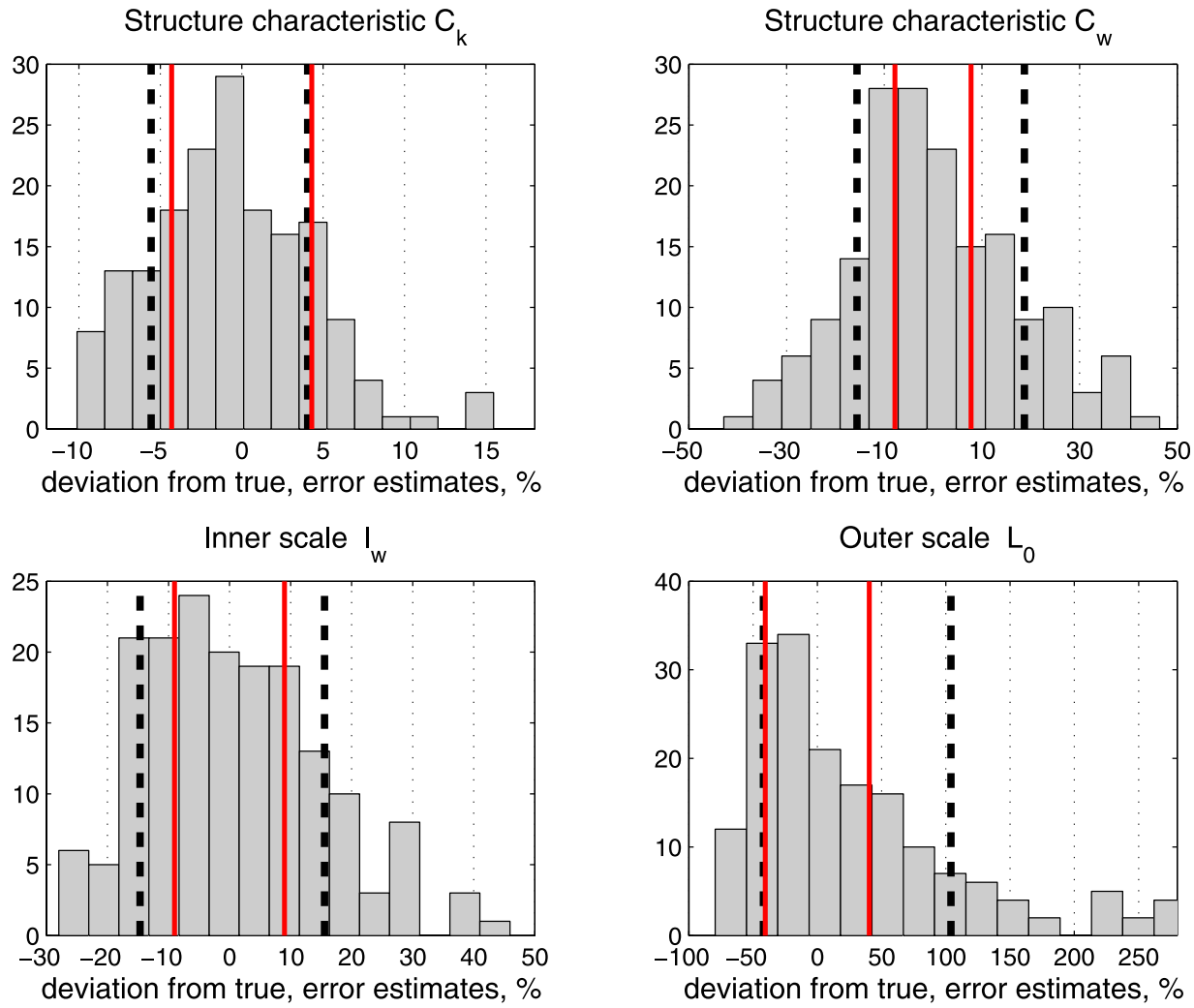

Figure 6. Histograms of relative deviations of the reconstructed parameters from the true ones. Dashed vertical lines are 0.16 and 0.84 percentiles; solid vertical lines indicate $\pm 1\sigma$ intervals obtained from the error estimates (19).

spectra parameters, as well as climatology studies, will be addressed in future publications after application of the methods discussed in this paper to a large GOMOS scintillation data set.

6.1. Successive Occultations of Sirius

[54] For an illustration of retrievals, we performed reconstruction of IGW and turbulence parameters for the series of 13 successive occultations of Sirius on 20 September 2002. The successive occultations are carried out at approximately the same latitude and local time (Table 1). The reconstructed parameters of IGW and turbulence spectra are presented in Figure 7. The accuracy of the retrievals for this occultation series is estimated to be ~5% at altitudes 25–45 km for l_W and 10–20% below 40 km and 20–40% above 40 km for L_0. Error estimates for C_K and C_W grow (nonlinearly) with altitude: they are ~5% at 30 km, ~20% at 40 km, and >50% above 45 km for C_W and ~ 15–20% at 30 km, ~30% at 40 km, and exceed 50% at altitudes above 45 km for C_K. Unreliable values of retrieved parameters (with error estimates exceeding 60% for C_K and C_W and 50% for L_0) were discarded; they are not shown in Figure 7. The bold lines in Figure 7 indicate the median profiles. The observed scattering of the retrieved parameters is rather due to the diversity of atmospheric states at different locations than

Table 1. Characteristics of Occultations of Star S001 (Sirius) Carried Out on 20 September 2002[a]

Orbit Number	Tangent Point at 30-km Altitude	UTC	SMLT	α
2904	35.7°S, 4.8°W	0:19	00:00	66.8°
2905	35.6°S, 30°W	2:00	00:00	66.9°
2906	35.3°S, 55.1°W	3:40	00:00	66.9°
2908	35.3°S, 105.5°W	7:01	23:59	67.1°
2910	34.8°S, 155.8°W	10:23	00:00	67.2°
2911	34.8°S, 179°E	12:03	23:59	67.2°
2912	34.0°S, 154°E	13:43	23:59	67.2°
2913	33.9°S, 128.9°E	15:24	00:00	67.3°
2914	33.8°S, 103.8°E	17:05	00:00	67.4°
2915	33.7°S, 78.8°E	18:45	00:00	67.4°
2916	33.6°S, 53.4°E	20:26	00:00	67.5°
2917	33.5°S, 28.2°E	22:06	23:59	67.5°
2918	33.4°S, 3°E	23:47	23:59	67.5°

[a]SMLT is solar mean local time.

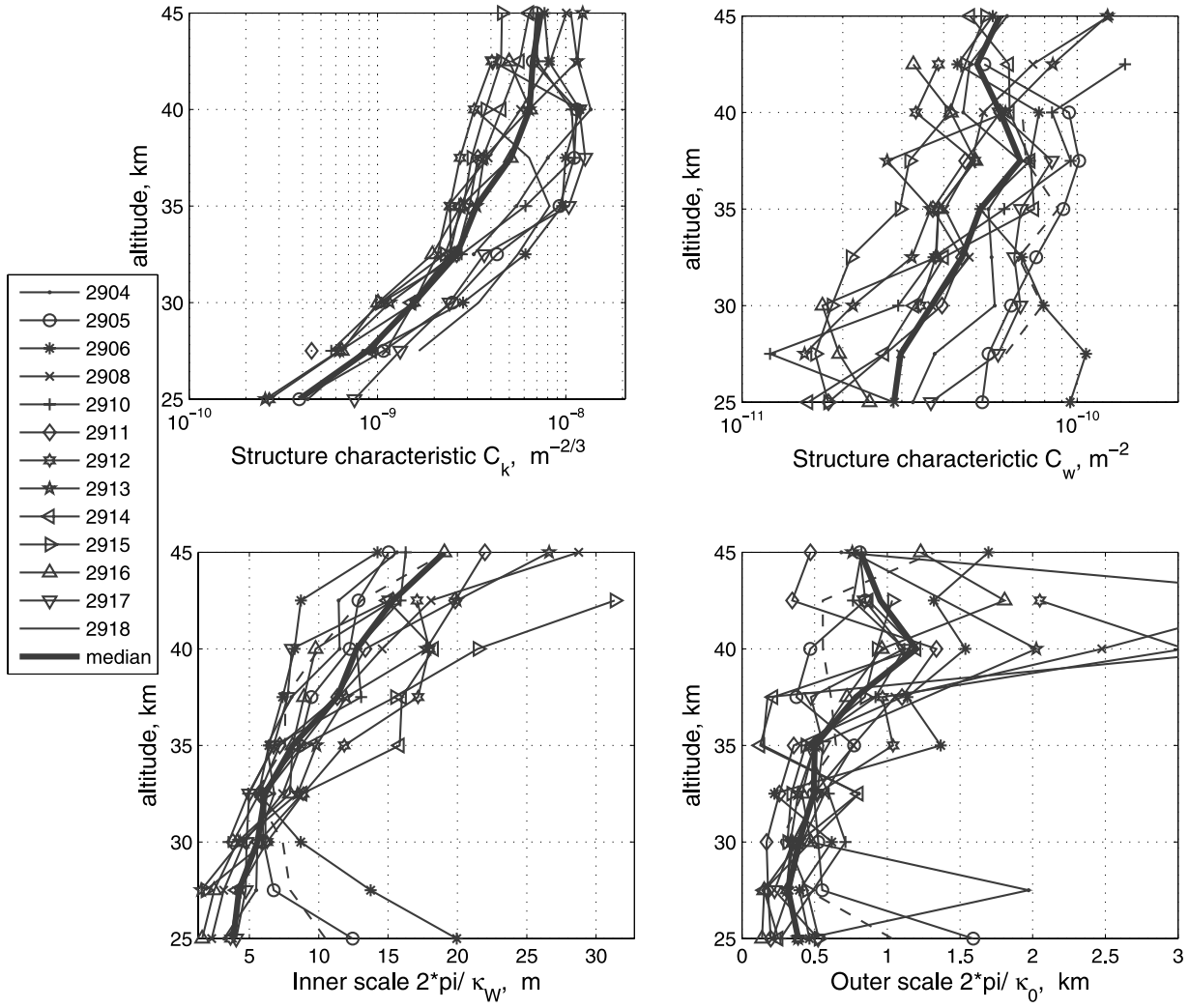

Figure 7. IGW and turbulence parameters from occultations R02904–2920/S001 (latitude ~35°S, $\alpha \sim 67°$, 20 September 2002). Heavy lines denote median profiles.

due to the uncertainty of the experimental spectra and retrievals. This diversity is also reflected in variations of scintillation intensity for different occultations.

[55] The structure characteristic C_W is nearly constant with altitude. The estimates of the constant A in equation (4), obtained by using the reconstructed values of C_W and ECMWF temperature profiles in occultation locations for estimates of the Brunt-Väisälä frequency, are $A \approx 0.09 \pm 0.02$. The statistics of the estimated parameters A (the median value and the 0.16 and 0.84 percentiles) is shown in Figure 8. The obtained estimates are in good agreement with the theoretical value $A = 0.1$ [*Tsuda et al.*, 1991] and with previous observational results using lidars [*Wilson et al.*, 1991], radiosondes [*Tsuda et al.*, 1991] and stellar scintillation measurements [*Gurvich and Kan*, 2003b].

[56] The turbulent structure characteristic C_K grows with altitude, with especially rapid increase at altitudes 25–35 km. These results are in qualitative and quantitative (taking into account the variability of retrieved parameters) agreements with previous retrievals from stellar scintillation measurements [*Gurvich and Kan*, 2003b]. The retrieved parameters C_K allow to compute the structure characteristic

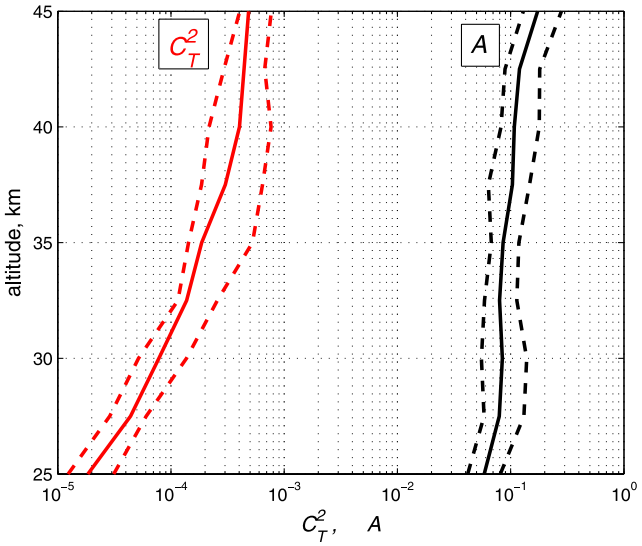

Figure 8. Parameters C_T^2 ($K^2\ m^{-2/3}$) and A (see text for explanation). Solid lines: median profiles; dashed lines: 0.16 and 0.84 percentiles.

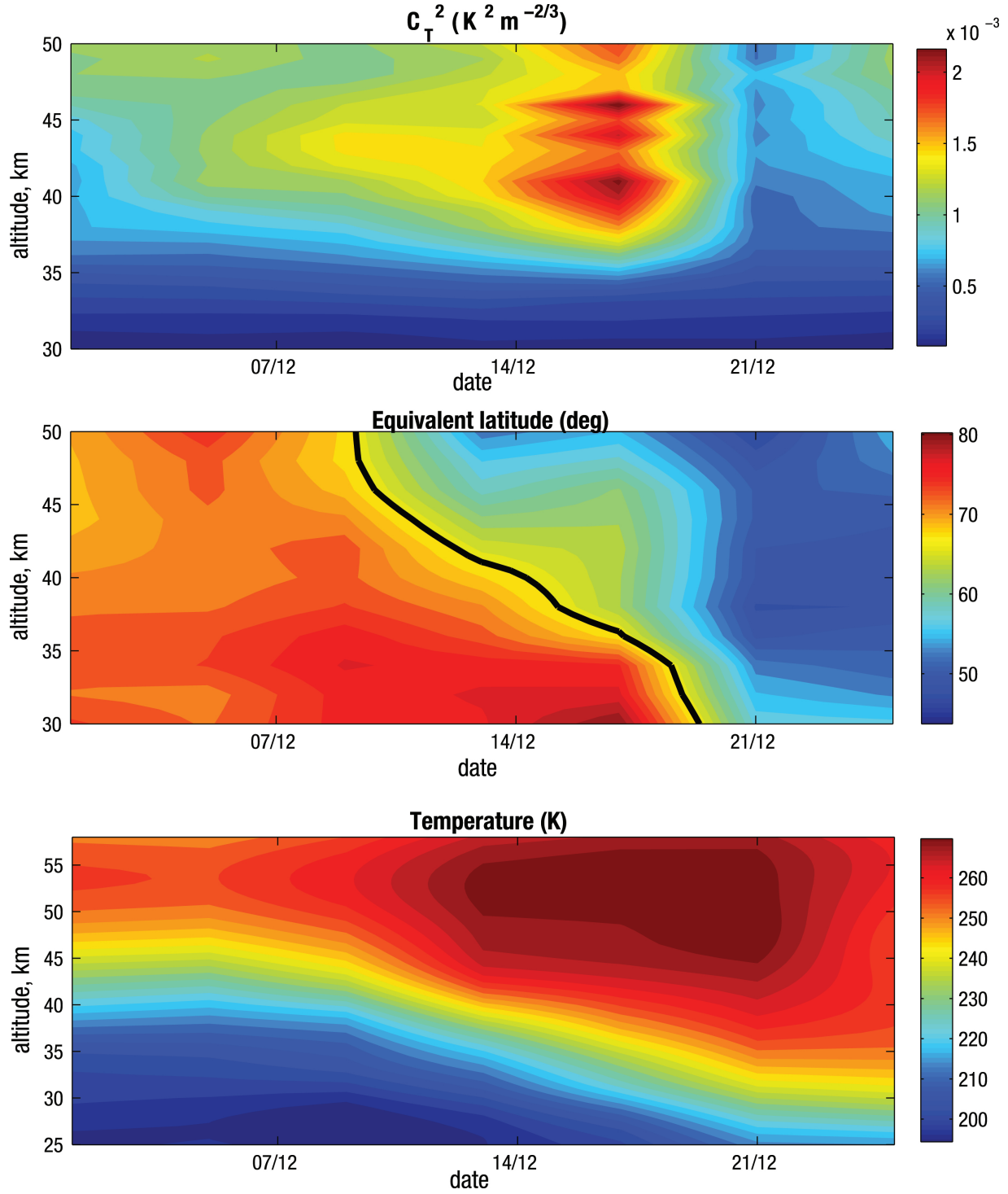

Figure 9. Top: C_T^2 in successive occultations of star 7 (visual magnitude 0.1, effective temperature 14,000 K) located at ~80°N in December 2003; 4-day zonal average data are presented. Middle: equivalent latitude at locations of the occultations computed using ECMWF data; the black line corresponds to 67° of equivalent latitude, which is used usually for indicating the polar vortex boundary. Bottom: temperature from ECMWF at latitude 80°N in December 2003.

of the isotropic component of the temperature fluctuation field $C_T^2 = \langle T \rangle^2 C_K$. The statistics of the estimates of C_T^2 (the median and 0.16 and 0.84 percentiles) is shown in Figure 8. At the lower limit of 25 km, the retrieved estimates are in agreement with the mean values of C_T^2 obtained from high-resolution balloon temperature measurements [*Gavrilov et al.*, 2005].

[57] The inner scale l_W grows with altitude, from 5–10 m at 30 km up to 20–30 m at 50 km. These values are consistent with the results previously obtained from stellar scintillations [*Gurvich and Kan*, 2003b; *Gurvich and Chunchuzov*, 2005].

[58] Despite large scattering in the retrieved outer-scale data, the outer scale is often well detected in scintillation spectra. The values of L_0 are in agreement with outer scales obtained with a similar method by *Gurvich and Chunchuzov* [2005]. The mean value of L_0 grows with altitude, from 0.5–1 km at 30 km up to 1–3 km at 45 km, thus being in qualitative agreement with the theoretical predictions that the dominant vertical scales should increase with altitude [*Fritts and Alexander*, 2003]. The retrieved values of outer scale, being in the range of the theoretical estimates for the L_0 possible values [*Gurvich and Chunchuzov*, 2005], are more than twice smaller than the values of the dominant vertical scale found by *Whiteway and Carswell* [1995] in temperature fluctuations from lidar measurements and by *Tsuda et al.* [1992] in the vertical wave number spectrum of horizontal wind fluctuations from rocket data. The explanation of this discrepancy, which relates it with the difference in methods for estimating the characteristic scales, is presented in the paper of *Gurvich and Chunchuzov* [2005]. The scintillation method averages the measured fluctuations over the extended atmospheric layer due to occultation geometry, thus the variances of density and wind speed fluctuations averaged over this layer may differ several times from their local values measured in some geographic regions. In addition, we should note that the scintillation method allows estimating the outer scale as a parameter that characterizes the deviation of the three-dimensional spectral density from a -5 power law at low wave numbers. A third possible reason of this discrepancy is that a bias toward small scales might be partially introduced by the retrieval method, which performs the retrievals of small, well-observed outer scale from scintillation measurements more accurately than that of large outer scale due to reasons discussed in section 5.

6.2. Evolution of C_T^2 at 80°N in December 2003

[59] For illustration of a larger data set, we followed the evolution of C_T^2 at 80°N during the stratospheric warming in December 2003. Figure 9 shows the time series of C_T^2 calculated using the reconstructed structure characteristics C_K (top) and ECMWF temperature data (bottom). In the beginning of December 2003, the occultations at 80°N are located mainly within the polar vortex (it is indicated by high values of equivalent latitude as shown in Figure 9, middle), and C_T^2 is relatively low at all considered altitudes. The beginning of the stratospheric warming on ~10 December is accompanied by the strong increase of C_T^2, which achieves its maximum on 14–21 December (the polar vortex has been broken down by 21 December, which is indicated by low values of equivalent latitude shown in Figure 9, middle). Sudden stratospheric warmings, caused by dissipation of planetary waves in the stratosphere, are characterized by very intensive mixing processes, which are detected by GOMOS observations. In addition, the breakdown of the polar vortex results in wind deceleration at higher altitudes, which in turn induces the IGW breaking and thus enhances turbulence. After the polar vortex breakdown (after 21 December), C_T^2 returns to usual values in the whole altitude range of 30–50 km.

7. Summary

[60] An algorithm for reconstruction of the parameters of internal gravity wave and turbulence spectra from the GOMOS scintillation measurements has been developed. The retrieval strategy is based on fitting the experimental scintillation spectra by the modeled ones. The modeling of scintillation spectra is based on a two-component model of air density irregularities: the first component corresponds to the gravity wave spectrum, while the second one describes isotropic turbulence resulting from internal gravity wave breaking. The retrieval of four parameters of IGW and turbulence spectra: the structure characteristics and the inner and the outer scales of the anisotropic spectrum, is based on the maximum likelihood method.

[61] The developed algorithm has been tested on simulated and real data, and its accuracy has been assessed. It has been shown that the measured scintillation spectra are in good agreement with the proposed model. It has been demonstrated that structure characteristics and inner and outer scales on the IGW component can be reconstructed from scintillation spectra at altitudes between 25 and 50 km. Sample retrievals from GOMOS scintillation measurements have shown that the retrieved parameters are in good agreement with previous analyses.

[62] Future application of the developed method opens possibility for obtaining information about global distribution of parameters of IGW and turbulence spectra in the stratosphere. The strength of the GOMOS scintillation measurements is that they cover the transition between the saturated part of the gravity wave spectrum and isotropic turbulence and might therefore allow visualizing the gravity wave breaking. This might be useful for validation of GW parameterization schemes used in general circulation models [*Charron et al.*, 2002].

[63] **Acknowledgments.** The authors thank the GOMOS team and ESA for the GOMOS data. The authors thank anonymous reviewers for their valuable comments. We gratefully acknowledge the insightful suggestion about the role of wind deceleration. The authors thank L. Backman and A. Seppälä, Finnish Meteorological Institute, for the help with equivalent latitude data. The work of V. F. Sofieva was supported by the Academy of Finland. The work of A. S. Gurvich was supported by the Russian Foundation for Basic Research, grant 06-05-64357.

References

Alexander, M. J. (1998), Interpretations of observed climatological patterns in stratospheric gravity wave variance, *J. Geophys. Res.*, *103*, 8627–8640.

Alexander, M. J., and J. R. Holton (1997), A model study of zonal forcing in the equatorial stratosphere by convectively induced gravity waves, *J. Atmos. Sci.*, *54*, 408–419.

Alexander, M. J., and K. Rosenlof (1996), Nonstationary gravity wave forcing of the stratospheric zonal mean wind, *J. Geophys. Res.*, *101*, 23,465–23,474.

Aleksandrov, A. P., G. M. Grechko, A. S. Gurvich, V. Kan, M. Kh. Manarov, A. I. Pakhomov, Yu V. Romanenko, S. A. Savchenko, S. I. Serova, and V. G. Titov (1990), Spectra of stratospheric temperature variations inferred from stellar scintillation observations from space, *Izv. Akad. Nauk SSSR Fiz. Atmos. Okeana*, *26*(1), 5–16.

Bertaux, J. L., et al. (2004), First results on GOMOS/Envisat, *Adv. Space Res.*, *33*, 1029–1035, doi:10.1016/j.asr.2003.09.037.

Carslaw, K., et al. (1998), Increased stratospheric ozone depletion due to mountain-induced atmospheric waves, *Nature*, *391*, 675–678.

Charron, M., E. Manzini, and C. D. Warner (2002), Intercomparison of gravity wave parameterizations: Hines Doppler-spread and Warner and McIntyre ultra-simple schemes, *J. Meteorol. Soc. Jpn.*, *80*, 335–345.

Dalaudier, F., and A. S. Gurvich (1997), A scalar three-dimensional spectral model with variable anisotropy, *J. Geophys. Res.*, *102*(16), 19,449–19,459.

Dalaudier, F., V. Kan, and A. S. Gurvich (2001), Chromatic refraction with global ozone monitoring by occultation of stars: I. Description and scintillation correction, *Appl. Opt.*, *40*, 866–877.

Dunkerton, T. J. (1997), The role of gravity waves in the quasi-biennial oscillation, *J. Geophys. Res.*, *102*, 26,053–26,076.

Dörnbrack, A., T. Birner, A. Fix, H. Flentje, A. Meister, H. Schmid, E. Browell, and M. Mahoney (2002), Evidence for inertia-gravity waves forming polar stratospheric clouds over Scandinavia, *J. Geophys. Res.*, *107*(D20), 8287, doi:10.1029/2001JD000452.

Eckermann, S. D., and P. Preusse (1999), Global measurements of stratospheric mountain waves from space, *Science*, *286*, 1534–1537.

Fritts, D. C., and M. J. Alexander (2003), Gravity wave dynamics and effects in the middle atmosphere, *Rev. Geophys.*, *41*(1), 1003, doi:10.1029/2001RG000106.

Fueglistaler, S., S. Buss, B. Luo, H. Wernli, H. Flentje, C. Hostetler, L. Poole, K. Carslaw, and T. Peter (2003), Detailed modeling of mountain wave PSCs, *Atmos. Chem. Phys.*, *3*, 697–712.

Garcia, R. R., and B. A. Boville (1994), "Downward control" of the mean meridional circulation and temperature distribution of the polar winter stratosphere, *J. Atmos. Sci.*, *51*, 2238–2245.

Gavrilov, N. M., H. Luce, M. Crochet, F. Dalaudier, and S. Fukao (2005), Turbulence parameter estimations from high-resolution balloon temperature measurements of the MUTSI-2000 campaign, *Ann. Geophys.*, *23*, 2401–2413.

Giorgetta, M., E. Manzini, and E. Roeckner (2002), Forcing of the quasi-biennial oscillation from a broad spectrum of atmospheric waves, *Geophys. Res. Lett.*, *29*(8), 1245, doi:10.1029/2002GL014756.

Grechko, G. M., A. S. Gurvich, V. Kan, S. V. Kireev, and S. A. Savchenko (1992), Anisotropy of spatial structures in the middle atmosphere, *Adv. Space Res.*, *12*(10), 169–175.

Gurvich, A. S. (1995), Model for the three-dimensional spectrum of locally axisymmetric temperature irregularities in a stably stratified atmosphere, *Izv. Atmos. Ocean. Phys.*, *31*(2), 211–216.

Gurvich, A. S. (1997), A heuristic model of three-dimensional spectra of temperature inhomogeneities in the stably stratified atmosphere, *Ann. Geophys.*, *15*(7), 856–869.

Gurvich, A. S., and V. L. Brekhovskikh (2001), Study of the turbulence and inner waves in the stratosphere based on the observations of stellar scintillations from space: A model of scintillation spectra, *Waves Random Media*, *11*, 163–181.

Gurvich, A., and I. Chunchuzov (2005), Estimates of characteristic scales in the spectrum of internal waves in the stratosphere obtained from space observations of stellar scintillations, *J. Geophys. Res.*, *110*, D03114, doi:10.1029/2004JD005199.

Gurvich, A. S., and V. Kan (2003a), Structure of air density irregularities in the stratosphere from spacecraft observations of stellar scintillation: 1. Three-dimensional spectrum model and recovery of its parameters, *Izv. Atmos. Ocean. Phys.*, *39*, 300–310.

Gurvich, A. S., and V. Kan (2003b), Structure of air density irregularities in the stratosphere from spacecraft observations of stellar scintillation: 2. Characteristic scales, structure characteristics, and kinetic energy dissipation, *Izv. Atmos. Ocean. Phys.*, *39*, 311–321.

Gurvich, A. S., et al. (2001a), Studying the turbulence and internal waves in the stratosphere from spacecraft observations of stellar scintillation: I. Experimental technique and analysis of the scintillation variance, *Izv. Atmos. Ocean. Phys.*, *37*(4), 436–451.

Gurvich, A. S., V. Kan, S. A. Savchenko, A. I. Pakhomov, and G. I. Padalka (2001b), Studying the turbulence and internal waves in the stratosphere from spacecraft observations of stellar scintillation: II. Probability distributions and scintillation spectra, *Izv. Atmos. Ocean. Phys.*, *37*(4), 452–465.

Gurvich, A. S., F. Dalaudier, and V. F. Sofieva (2005), Study of stratospheric air density irregularities based on two-wavelength observation of stellar scintillation by Global Ozone Monitoring by Occultation of Stars (GOMOS) on Envisat, *J. Geophys. Res.*, *110*, D11110, doi:10.1029/2004JD005536.

Holton, J. R. (1983), The influence of gravity wave breaking on the general circulation of the middle atmosphere, *J. Atmos. Sci.*, *40*, 2497–2507.

Jensen, E., L. Pfister, A. Ackerman, A. Tabazadeh, and O. Toon (2001), A conceptual model of the dehydration of air due to freeze-drying by optically thin, laminar cirrus rising slowly across the tropical tropopause, *J. Geophys. Res.*, *106*, 17,237–17,252.

Jiang, J. H., S. D. Eckermann, D. L. Wu, and J. Ma (2004a), A search for mountain waves in MLS stratospheric limb radiances from the winter Northern Hemisphere: Data analysis and global mountain wave modeling, *J. Geophys. Res.*, *109*, D03107, doi:10.1029/2003JD003974.

Jiang, J. H., B. Wang, K. Goya, K. Hocke, S. D. Eckermann, J. Ma, D. L. Wu, and W. J. Read (2004b), Geographical distribution and interseasonal variability of tropical deep convection: UARS MLS observations and analyses, *J. Geophys. Res.*, *109*, D03111, doi:10.1029/2003JD003756.

Kan, V. (2004), Coherence and correlation of chromatic stellar scintillations in a spaceborne occultation experiment, *Izv. Atmos. Ocean. Opt.*, *17*, 725–735.

Kyrölä, E., et al. (2004), GOMOS on Envisat: An overview, *Adv. Space Res.*, *33*, 1020–1028, doi:10.1016/S0273-1177(03)00590-8.

Monin, A. S., and A. M. Yaglom (1975), *Statistical Fluid Mechanics*, vol. 2, MIT Press, Cambridge, Mass.

Press, W. H., S. A. Teukolsky, W. T. Vetterling, and B. P. Flannery (1992), *Numerical Recipes in FORTRAN: The Art of Scientific Computing*, Clarendon, Oxford, U. K.

Preusse, P., A. Dörnbrack, S. D. Eckermann, M. Riese, B. Schaeler, J. Bacmeister, D. Broutman, and K. U. Grossmann (2002), Space-based measurements of stratospheric mountain waves by CRISTA: 1. Sensitivity, analysis method and a case study, *J. Geophys. Res.*, *107*(D23), 8178, doi:10.1029/2001JD000699.

Sidi, C., J. Lefrere, F. Dalaudier, and J. Barat (1988), An improved atmospheric buoyancy wave spectrum model, *J. Geophys. Res.*, *93*(1), 774–790.

Smith, S. A., D. C. Fritts, and T. E. VanZandt (1987), Evidence of a saturation spectrum of atmospheric gravity waves, *J. Atmos. Sci.*, *44*(10), 1404–1410.

Steiner, A. K., and G. Kirchengast (2000), Gravity wave spectra from GPS/MET occultation observations, *J. Atmos. Ocean. Technol.*, *17*, 495–503.

Takahashi, M. (1996), Simulation of the stratospheric quasi-biennial oscillation using a general circulation model, *Geophys. Res. Lett.*, *23*, 661–664.

Tamminen, J. (2004), Adaptive Markov chain Monte Carlo algorithms with geophysical applications, Finnish Meteorological Institute Contributions, No.47, Ph.D. thesis, Univ. of Helsinki.

Tatarskii, V. I. (1971), *The Effects of the Turbulent Atmosphere on Wave Propagation*, 417 pp., US Dep. of Commer., Washington, D. C.

Tsuda, T., T. E. VanZandt, M. Mizumoto, S. Kato, and S. Fukao (1991), Spectral analysis of temperature and Brunt–Väisälä frequency fluctuations observed by radiosondes, *J. Geophys. Res.*, *96*(9), 17,265–17,278.

Tsuda, T., K.-I. Oyama, Y. Murayama, H. Kanzawa, T. Nakamura, M. D. Yamanaka, S. Fukao, and S. Kato (1992), Characteristics of gravity waves in the middle atmosphere observed with rocketsondes at Uchinoura during DYANA campaign, paper presented at International Symposium on Middle Atmospheric Science, Radio Atmos. Sci. Cent., Kyoto Univ., Kyoto, Japan.

Tsuda, T., M. Nishida, C. Rocken, and R. H. Ware (2000), A global morphology of gravity wave activity in the stratosphere revealed by the GPS occultation data (GPS/MET), *J. Geophys. Res.*, *105*(D6), 7257–7273.

Whiteway, J. A., and A. I. Carswell (1995), Lidar observations of gravity wave activity in the upper stratosphere over Toronto, *J. Geophys. Res.*, *100*, 14,113–14,124.

Wilson, R., M.-L. Chanin, and A. Hauchecorne (1991), Gravity waves in the middle atmosphere observed by Rayleigh lidar: Part 2. Climatology, *J. Geophys. Res.*, *96*, 5169–5183.

Wu, D. L., and F. Zhang (2004), A study of mesoscale gravity waves over the North Atlantic with satellite observations and a mesoscale model, *J. Geophys. Res.*, *109*, D22104, doi:10.1029/2004JD005090.

Wu, D. L., P. Preusse, S. D. Eckermann, J. H. Jiang, M. de la Torre Juarez, L. Coy, B. Lawrence, and D. Y. Wang (2006), Remote sounding of atmospheric gravity waves with satellite limb and nadir techniques, *Adv. Space Res.*, doi:10.1016/j.asr.2005.07.031.

Yaglom, A. M. (1987), *Correlation Theory of Stationary and Related Random Functions*, Springer New York.

F. Dalaudier, Service d'Aeronomie, Verrières-le-Buisson Cedex, France.

A. S. Gurvich and V. Kan, A. M. Oboukhov Institute of Atmospheric Physics, Moscow, Russia.

V. F. Sofieva, Finnish Meteorological Institute, Geophysical research, P.O. Box 503, Vuorikatu 15a Helsinki FIN-00101, Finland. (viktoria.sofieva@fmi.fi)